Mechanical properties modeling of severely plastically deformed biodegradable ZK60 magnesium alloy for bone implants

Yan Zhang[a] , Ning Wang[b] , Jingyi Li[c] , Mohsen Mesbah[d] , Kuan Yew Wong[e] , Alireza Fallahpour[e] , Bahman Nasiri-Tabrizi[f] , Jiangfei Yang[b]*

[a] Department of Trauma Orthopedics, Shandong Provincial Hospital Affiliated to Shandong First Medical University, Jinan, Shandong Province, 250021, China. E-mail: doctorzhangyan1@sina.com
[b] Radiology Department, Shandong Provincial Hospital Affiliated to Shandong First Medical University, No.324 Jingwu Road, Huaiyin District, Jinan, Shandong 250000, China. E-mail: wnxtt1234@sina.com, yangjiangfei9120@sina.com
[c] Operation room, The Affiliated Hospital of Qingdao University, Huangdao District, Qingdao, Shandong province, 266000, China. E-mail: Grc7729@sina.com
[d] Department of Mechanical Engineering, Faculty of Engineering, University of Malaya, 50603 Kuala Lumpur, Malaysia. E-mail: mohsen_mesbah2005@yahoo.com
[e] School of Mechanical Engineering, Universiti Teknologi Malaysia, 81310 Skudai, Malaysia. E-mail: wongky@mail.fkm.utm.my, fallahpour.a@gmail.com
[f] School of Biosciences, Faculty of Health and Medical Sciences, Taylor's University, Subang Jaya, Malaysia. E-mail: b.nasiritabrizi@gmail.com

* Corresponding author

https://doi.org/10.1590/1679-78256151

Abstract

The effectiveness of magnesium (Mg) alloys to improve the capability of bone tissue generation may be severely diminished if the required mechanical properties are not provided. Here, the effort is directed to model the mechanical performance of severely plastically deformed biodegradable ZK60 Mg alloy in bone regeneration protocols. For this purpose, the effects of parallel tubular channel angular pressing (PTCAP) on yield strength (σ_{YS}), ultimate tensile strength (σ_{UTS}), and elongation to failure (δ) were addressed. Given the multifaceted variables of the PTCAP with nonlinear interactions, a precise determination of the mechanical properties requires a large number of experiments. Therefore, gene expression programming (GEP) and genetic programming (GP) models were proposed to achieve appropriate combinations of mechanical properties for bone implant purposes based on a rational hypothesis that for correlation coefficient ($|R|$) higher than 0.8, a strong correlation is established between the predicted and measured values. The results verified that the highest mechanical performance was achieved at the second pass of PTCAP, thus has a great potential to be the most promising candidate for biodegradable implant material. Besides, the proposed models were capable of precisely predicting the mechanical performance of the SPD-processed biodegradable ZK60 Mg.

Keywords

severe plastic deformation (SPD); mechanical properties; biodegradable bone implants; prediction; machine learning (ML)

Graphical Abstract
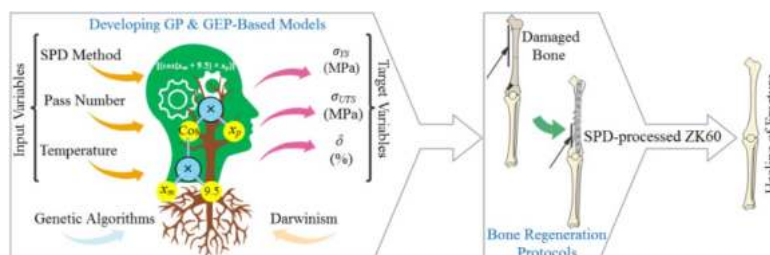
1 INTRODUCTION

The substantial advancement in medical devices has noticeably improved the quality and longevity of human life. The medical devices involve various medical implants, which cover an extensive range of applications, e.g., artificial joints, stents, pacemakers, and lap-bands with the main aim to support tissue regeneration and provide optimal healing (Bazaka and Jacob, 2013). In this context, the utilization of bioresorbable implants is increasing and contending with more conventional titanium (Ti)-based implants (Yang et al., 2018). Polymeric implants have been used for several years as bioresorbable materials, but Mg-based alloys now offer an improved option. Accordingly, more recent developments within the bioresorbable implants market include Mg-based alloys because they present innovatory solutions and have higher biological efficiency (Chakraborty Banerjee et al., 2019). Besides, these alloys have attracted much attention due to their attractive properties compared to polymeric implants, such as mechanical characteristics similar to those of bone, degradation in body fluid, and ability to motivate the development of new bones (Dargusch et al., 2020). This suggests that Mg-based alloys are much more suited for use in orthopedic implants. However, some of their weak points, for instance highly anisotropic mechanical behavior, inadequate mechanical strength, and elongation to failure must be taken into account before applying for bone implants. These weaknesses can be addressed through various manufacturing strategies like severe plastic deformation (SPD) processes (Gopi, 2020; Kim et al., 2020; Yan et al., 2020), where the composition and the manufacturing process method must be chosen very carefully with regard to the necessities of an application.

Several SPD processes, such as accumulative roll bonding (ARB) (Rao et al., 2019), high-pressure torsion (HPT) (Figueiredo and Langdon, 2019), equal channel angular pressing (ECAP) (Martynenko et al., 2019), and tubular channel angular pressing (TCAP) (Reshadi et al., 2015) are introduced as encouraging approaches for fabricating UFGs Mg-based alloys. Aside from these common methods, PTCAP is also made known as a new SPD technique for the fabrication of UFGs and nanostructured tubes, in which the deformation entails two half-cycles that are affected by a range of processing parameters involving deformation ratio, curvature angle and channel angle (Kasaeian-Naeini et al., 2019; Mesbah et al., 2016a; Mesbah et al., 2019). However, considering the multifarious factors of the SPD techniques with nonlinear interrelations, an accurate determination of the material features necessitates a large number of tests, which is not industrially and commercially cost-effective (Mesbah, 2013; Mesbah et al., 2014; Mesbah et al., 2016b; Wang et al., 2020). Therefore, to accurately examine the in vitro and in vivo performance of severely plastically deformed biodegradable Mg-based alloys, it is essential to model the mechanical properties of the processed alloys using more advanced machine learning (ML) schemes including Artificial Neural Networks (ANNs) (Bahrami-Karkevandi et al., 2019), Decision Trees (DTs) (Blanco-Justicia et al., 2020), Support Vector Machines (SVMs) (Land and Schaffer, 2020), Regression Analysis (RA) (Itano et al., 2020), Bayesian Networks (BNs) (McLachlan et al., 2020), and Genetic Algorithms (GAs) (Davis, 1991). In these techniques, executing ML includes constructing a model that is trained on the training dataset and subsequently can process residual data to generate accurate predictions (Mueller et al., 2016; Rafieerad et al., 2016; Rafieerad et al., 2017).

It has been over a decade since the notion that the merging of nanotechnology and ML will make further progress in the healthcare industry. In this regard, nanotechnology unites a range of scientific disciplines covering physics, chemistry, engineering, and biology, whereas ML can construct mathematical models based on specimen data to make predictions or decisions without being expressly planned to do the task (Adir et al., 2019; Azimi-Pour and Eskandari-Naddaf, 2018; Jones et al., 2016; Sacha and Varona, 2013). This suggests that creating a proper linkage between the nanotechnology and ML can advance modeling of biomechanical response, design of medical implants, and clinical treatment, whereby technological excellence in medical care will be achieved (González-Durruthy et al., 2017; Heller et al., 2019). However, the maturation of this interdisciplinary approach requires a great deal of research in various aspects of fabrication, characterization, and performance evaluation of the advanced materials, particularly medical implants with improved design and biofunctionality (Cilla et al., 2017).

Although there are numerous studies on SPD fabrication and refinement of various biodegradable Mg-based alloys and their impacts on microstructural evolution, the link between SPD processing parameters and the precise formulation of the mechanical behavior is not clear yet. In fact, most of the previous studies just focused on the microstructural and mechanical characterization (Khoubrou et al., 2020; Kim et al., 2009; Mueller and Mueller, 2007), regardless of the importance of properties modeling of the SPD-processed Mg-based alloys in industrial design, aimed at developing improved medical implants based on nanotechnology. Therefore, the present study aims to develop appropriate GEP and GP models for estimating the mechanical behavior of the SPD-processed biodegradable ZK60 Mg alloy, where the capability of the GAs versus restricted training dataset was addressed in detail for the first time. Here, the SPD method, number of the pass, and processing temperature were considered as input parameters to estimate the mechanical performance of the processed biodegradable Mg alloy as output.

2 MATERIALS AND METHODS

2.1 ZK60 Mg alloy

The ZK60 Mg alloy with a chemical composition of Mg–5.5Zn–0.5Zr–0.025Mn–0.025Al (wt%) was purchased as an extruded bar and it was then machined into cylindrical workpieces with 40 mm length, 20 mm external diameter, and 2.5 mm thickness.

2.2 Fabrication method and the concept of a biodegradable implant

The details of the fabrication and characterization of the UFG ZK60 Mg are described elsewhere (Mesbah et al., 2019). In brief, a particular die with a φ_i channel as well as $\Psi_1 = 150°$ and $\Psi_2 = 0°$ curvature angles were made-up from hot-worked tool steel H13 hardened to 55 HRC, followed by the PTCAP using an INSTRON press machine. The specimens were subjected to PTCAP up to three passes at 300 °C with a ram speed of 5 mm min^{-1}, wherein molybdenum disulfide (MoS$_2$) was used as an inorganic lubricant to lessen the friction of the substance against the die.

Schematic representation of the PTCAP procedure including preliminary status, first half-cycle, second half-cycle along with the die parameters, and an example of ZK60 Mg alloy after three-pass is shown in Figure 1. As illustrated in this figure, by applying the primary punch in the right direction, the cylindrical workpieces are driven into the deformation region during SPD-induced structural refinement that is composed of a tubular channel with two shear zones. The cylindrical workpieces are then pressed rearward into the same shear zones through the next punch to regain their initial size. It should be mentioned that tensile circumferential strain is achieved during the first half cycle, while within the second half cycle compression circumferential strain is gained. In this process, the overall accumulated plastic strain can be calculated based on the number of passes, channel angles, and curvature angles (Mesbah et al., 2019), where equivalent plastic strains of 1.8 and 5.4 were specified following the first and third passes of PTCAP, respectively.
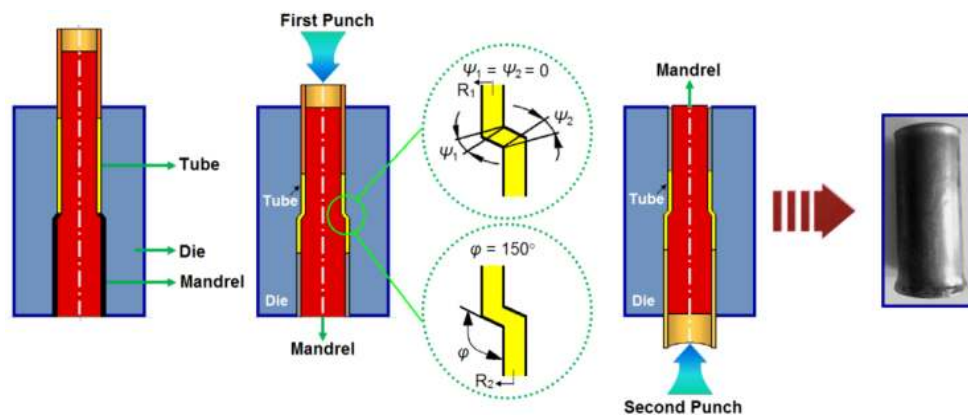

Figure 1. Schematic representation of the PTCAP procedure including preliminary status, first half-cycle, second half-cycle along with the die parameters, and ZK60 Mg alloy after three-pass.

On the other hand, various problematic clinical situations can be addressed by the expansion of novel concepts, instruments, and medical implant design for surgical trials and exploration in orthopedics-traumatology. Figure 2 shows the human skeleton and the implantation of biodegradable ZK60 Mg alloy into the bone defects, wherein just the treatment of forearm and femur bones is presented as examples. In this concept, several factors have to be taken into consideration based on the highest standard, such as surgical decision making, implant positioning, reinforcement mechanisms, and evaluation of bone healing. For instance, in some cases (femur bone fractures), the favored treatment is the interior fixation with lag screws and/or cerclage wires and sealing the fracture line, coupled with a neutralization plate, wherein the screws/wires employed throughout the fracture make friction between the parts and counteract shearing forces, whereas the neutralization plate safeguards the stability from failing (Agarwala et al., 2017). This suggests that the mechanical strength of the medical implants must be tuned to meet the needs of tissue regeneration. Besides, the modulus of elasticity of Mg-based alloys are in the range of 40 to 45 GPa, which is well-matched with the natural bone stiffness (3–20 GPa), whereby can reduce the stress shielding effect as compared to usual metallic implants like titanium (Ti)-based alloys (~115 GPa), cobalt (Co)-based alloys (~230 GPa), and stainless steel (~200 GPa) (Kamrani and Fleck, 2019). Thus, the main focus here is only on estimating the mechanical features of the SPD-processed biodegradable ZK60 Mg alloy. It is also very important to note that the biodegradable implant should degrade at a rate fitted to tissue recovering, idyllically diminishing its mechanical strength in a manner harmonizing with an increment in

the load-bearing capability of the supporting tissue, as well as sustaining the mechanical entirety until the tissue has healed perfectly. In this respect, Mg^{2+} ions, which leak out throughout degradation, consume metabolically without any side effects and toxicity (Ding, 2016; Wang et al., 2019).
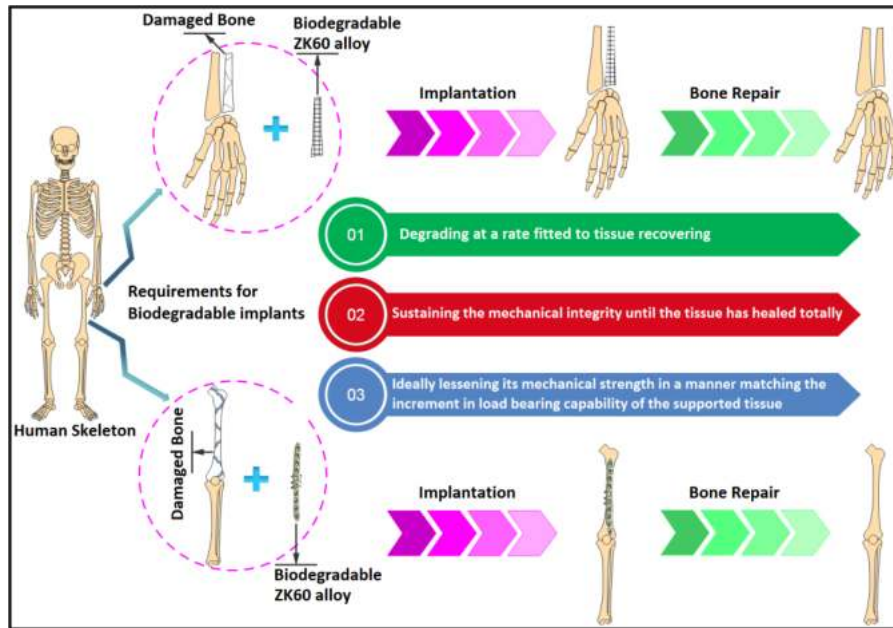

Figure 2. Human skeleton and the implantation of biodegradable ZK60 Mg alloy into the bone defects. Here, only the treatment of forearm and femur bones is presented.

2.3 Mechanical behavior modeling

With the aim of material design, the most important step is to create an interaction model that can precisely portray the connection between the input material characteristics or processing parameters and the desired properties based on a certain dataset. The creation of traditional models is greatly dependent on physical intuition and procedures, for instance, utilizing energy conservation as well as thermodynamics laws to develop mathematical equations with typically linear or somewhat nonlinear parameters regressed from available reference data. In contrast, in ML training the model is done in a particular path using an elastic and commonly nonlinear form only from accessible data sources (Picklum and Beetz, 2019; Schmidt et al., 2019; Wei et al., 2019; Zhou et al., 2019).

In the field of materials science and engineering, there are commonly multifaceted interactions between the configuration of a material and the favorite features; which are arduous to handle through conventional correlation schemes. Consequently, ML algorithms came into sight as a potential method for estimating the material properties as well as for optimum design purposes and materials screening. In this section, a general workflow for mechanical behavior modeling of biodegradable Mg-based alloys based on ML methods, involving descriptor generation and dimensionality reduction, model creation, and validation, as well as prediction of mechanical properties (i.e. δ, σ_{YS}, and σ_{UTS}) and verification of the experimental outputs is presented. This general workflow is shown in Figure 3, which includes the following steps:

- The primary phase is to denote a numerical dataset of distinct material using a series of features (descriptors) and thus necessitates certain discipline knowledge about the grade and applications of materials. Zn is known as an extremely necessary element for humans so that almost all the physiological activities are intensely disturbed in its deficiency. On the other hand, Zr has a set of proper features for orthopedic purposes, e.g., high corrosion resistance, low specific weight, as well as biocompatibility (Lu et al., 2012). Accordingly, ZK series alloys, in particular, ZK40 and ZK60, have recently received considerable interest owing to their biocompatibility and biosafety (Liu et al., 2018). This suggests that ZK60 Mg alloy is a promising candidate for biodegradable metal implants for use in bone repair therapies (Byun et al., 2020). Based on the above considerations, ZK60 Mg alloy was chosen in the present study. Thus, as demonstrated in Figure 3, in the present case, a numerical dataset of the SPD-processed ZK60 Mg alloy and specific insight in mechanical behavior (i.e., σ_{YS}, σ_{UTS}, and δ) and its potential applications in implantology is required. Here, the mechanical behavior of the processed ZK60 Mg alloy was

examined using the load-displacement data, which collected from each run and converted into the engineering stress-strain curve, where elongation to failure was determined through the curves obtained.

- The second phase is to create a sketching model between the descriptors and the objective characteristics based on recognized data for a set of reference materials, where a variety of ML techniques, such as ANNs (Bahrami-Karkevandi et al., 2019), DTs (Blanco-Justicia et al., 2020), SVMs (Land and Schaffer, 2020), RA (Itano et al., 2020), BNs (McLachlan et al., 2020), and GAs (Davis, 1991) can be employed. Here, GEP as a population-based progressive algorithm was established, wherein individuals were encoded as linear strings of fixed size (genome). Besides, GP has been used, as the first extended perfectly matched layer (EPML) technique, to show the estimation power of the developed GEP models.

- In the third phase, the reverse design is done to acquire new structures with favorite performance derived from the developed ML-based models and the most encouraging candidate can eventually be fabricated and its actual features can be established on trial (Zhou et al., 2019). Here, the model comparison plots of the estimated values against the real data are presented in support of GEP and GP models for δ, σ_{YS}, and σ_{UTS}.
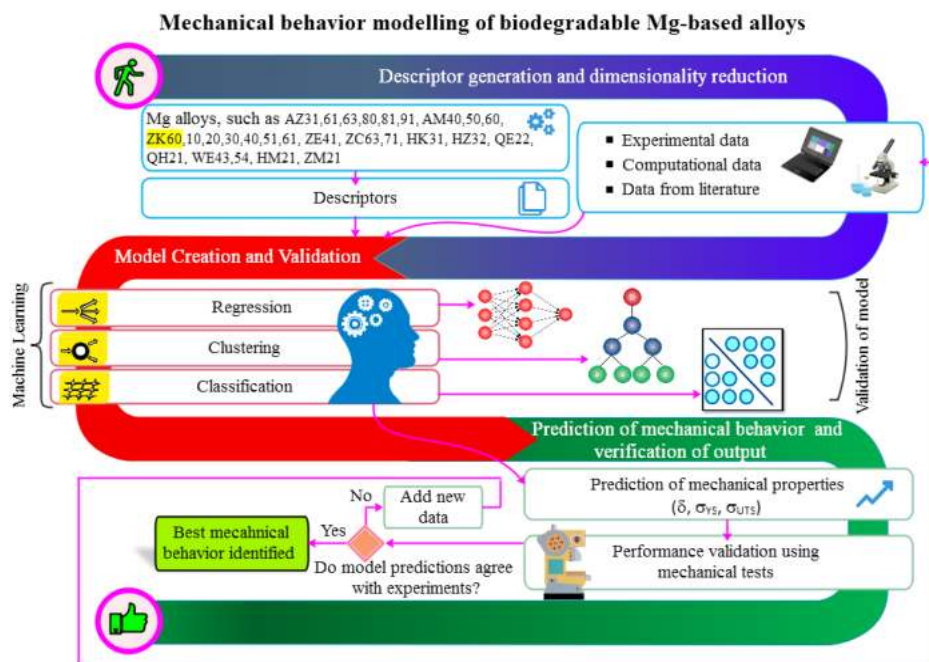

Figure 3. A general workflow for mechanical behavior modeling of biodegradable Mg-based alloys based on ML methods, involving descriptor generation and dimensionality reduction, model creation and validation, as well as prediction of mechanical properties (i.e., δ, σ_{YS}, and σ_{UTS}) and verification of the experimental outputs.

The limit values of input and output variables used in the GEP and GP models are summarized in Table 1. It should be noted that further details on input and output variables can be found in the literature (Dumitru et al., 2014; He et al., 2010; Mostaed et al., 2014; Orlov et al., 2011; Vinogradov, 2017).

Table 1. The limit values of input and output variables.

	Minimum	Maximum
	Data used in the GP and GEP models	
Input Parameters		
SPD Method	M1	M3
The number of passes	0	8
Temperature (K)	273	573
Output Parameters		
δ (%)	4	35.1
σ_{YS} (MPa)	120	320
σ_{UTS} (MPa)	221	397

3 RESULTS

3.1 Mechanical properties of ZK60 Mg alloy

Figure 4 shows the radar charts of the mechanical properties (δ (%), σ_{YS} (MPa), and σ_{UTS} (MPa)) of the SPD-processed biodegradable ZK60 Mg alloy based on the used dataset, which is collected from our previous work (Mesbah et al., 2019) and the relevant literature (Dumitru et al., 2014; He et al., 2010; Mostaed et al., 2014; Orlov et al., 2011; Vinogradov, 2017). The corresponding dataset is summarized in Table 2. Since the main objective of the present study is on modeling the mechanical behavior of severely plastically deformed biodegradable ZK60 Mg alloy, the dataset includes only the values obtained from processed ZK60 Mg alloy by different SPD methods, including PTCAP, ECAP, and HRDSR, where the type of SPD process, number of the pass, and processing temperature were considered as input parameters to model the mechanical behavior of the processed biodegradable ZK60 Mg alloy as output. Based on Figure 4 as well as Table 2, higher mechanical strength was observed at the second PTCAP pass as compared to the results of the tensile test of the unprocessed and other processed ZK60 Mg alloy.
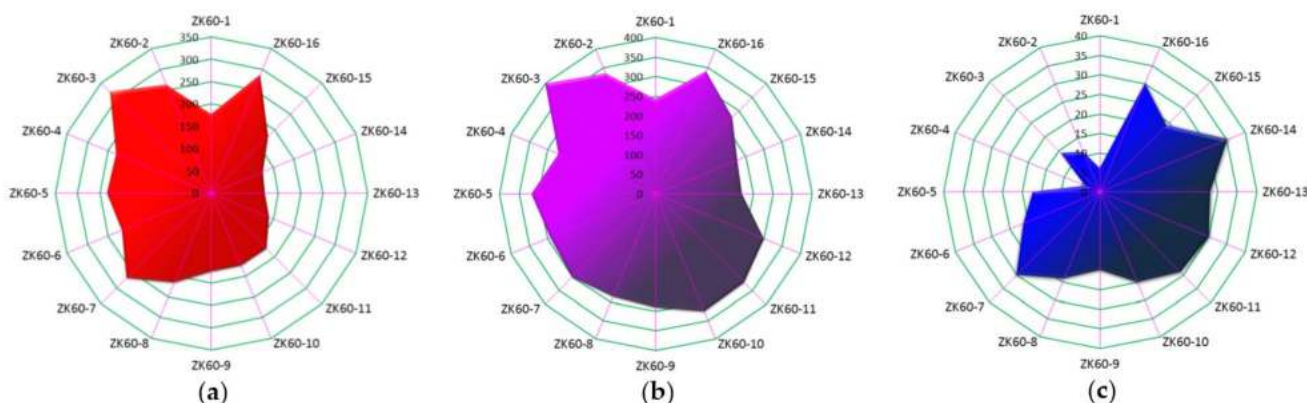

Figure 4. Radar charts of the mechanical properties of the SPD-processed biodegradable ZK60 Mg alloy (**a**) σ_{YS} (MPa), (**b**) σ_{UTS} (MPa), and (**c**) δ (%) based on the used dataset.

Table 2. The collected dataset from our prior findings (Mesbah et al., 2019) and the literature (Dumitru et al., 2014; He et al., 2010; Mostaed et al., 2014; Orlov et al., 2011; Vinogradov, 2017).

Alloy	Input Parameters			Output Parameters			Ref.
	SPD Method	Pass	T (K)	δ (%)	σ_{YS} (MPa)	σ_{UTS} (MPa)	
ZK60-1	M1 [1]	0	273	6	176	241	(Mesbah et al., 2019)
ZK60-2	M1	1	573	11	262	332	(Mesbah et al., 2019)
ZK60-3	M1	2	573	14	320	397	(Mesbah et al., 2019)
ZK60-4	M1	3	573	4	230	267	(Mesbah et al., 2019)
ZK60-5	M2 [2]	4	523	17	233	316	(Dumitru et al., 2014; He et al., 2010; Mostaed et al., 2014; Orlov et al., 2011; Vinogradov, 2017)
ZK60-6	M2	4	473	21	216	290	(Dumitru et al., 2014; He et al., 2010; Mostaed et al., 2014; Orlov et al., 2011; Vinogradov, 2017)
ZK60-7	M2	4	423	30	268	300	(Dumitru et al., 2014; He et al., 2010; Mostaed et al., 2014; Orlov et al., 2011; Vinogradov, 2017)
ZK60-8	M2	8	423	24	216	283	(Dumitru et al., 2014; He et al., 2010; Mostaed et al., 2014; Orlov et al., 2011; Vinogradov, 2017)
ZK60-9	M2	1	523	20	175	290	(Dumitru et al., 2014; He et al., 2010; Mostaed et al., 2014; Orlov et al., 2011; Vinogradov, 2017)
ZK60-10	M2	2	523	25	175	325	(Dumitru et al., 2014; He et al., 2010; Mostaed et al., 2014; Orlov et al., 2011; Vinogradov, 2017)
ZK60-11	M2	3	523	29	175	320	(Dumitru et al., 2014; He et al., 2010; Mostaed et al., 2014; Orlov et al., 2011; Vinogradov, 2017)
ZK60-12	M2	4	523	30	140	300	(Dumitru et al., 2014; He et al., 2010; Mostaed et al., 2014; Orlov et al., 2011; Vinogradov, 2017)

Table 2. Continued...

Alloy	Input Parameters			Output Parameters			Ref.
	SPD Method	Pass	T (K)	δ (%)	σ_{YS} (MPa)	σ_{UTS} (MPa)	
ZK60-13	M2	4	513	28.1	120	221	(Dumitru et al., 2014; He et al., 2010; Mostaed et al., 2014; Orlov et al., 2011; Vinogradov, 2017)
ZK60-14	M2	8	513	35.1	125	226	(Dumitru et al., 2014; He et al., 2010; Mostaed et al., 2014; Orlov et al., 2011; Vinogradov, 2017)
ZK60-15	M2	2	523	24	180	277	(Dumitru et al., 2014; He et al., 2010; Mostaed et al., 2014; Orlov et al., 2011; Vinogradov, 2017)
ZK60-16	M3 [3]	1	473	30	286	338	(Dumitru et al., 2014; He et al., 2010; Mostaed et al., 2014; Orlov et al., 2011; Vinogradov, 2017)

[1] PTCAP parallel tubular-channel angular pressing; [2] ECAP equal channel angular pressing; [3] HRDSR high-ratio differential speed rolling

3.2 Predictive modeling construction for mechanical behavior of biodegradable ZK60 Mg alloy

In this section, the GP and GEP-based mathematical models are developed for use in the mechanical assessment of the SPD-processed biodegradable ZK60 Mg alloy aimed at enhancing mechanical integrity for temporary metallic implants. For preparing a good dataset, it is essential to consider those parameters that have the greatest effect on the system performance. In the present study, the method of SPD (x_m), number of passes (x_p), and temperature of the manufacturing process (x_{tk}) are among the most important parameters that influence the mechanical properties of the processed ZK60 Mg alloy, as demonstrated in Figure 5. All these parameters mentioned in Table 2, are introduced to the models as the input parameters, while σ_{YS}, σ_{UTS}, and δ that are designated as the performance symbols, are considered as the output parameters. Here, the GP and GEP models make a relationship between all the input parameters and the output. This relationship as the harvest of the GP and GEP models is provided in the form of expression trees (ETs) as illustrated in Figures 6, 7, 8, 10, 11, and 12, which is translated into a mathematical formula as explained in the following paragraphs.
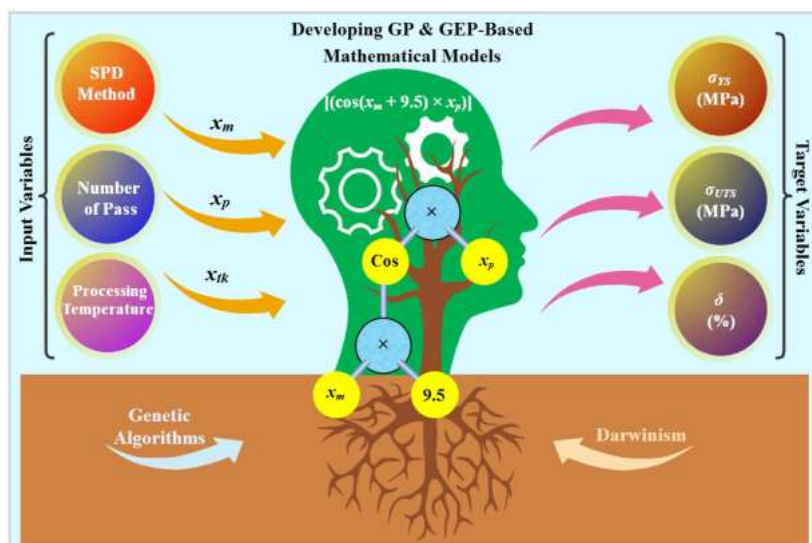

Figure 5. Developing GP and GEP-based mathematical models for the mechanical behavior of the SPD-processed biodegradable ZK60 Mg alloy.

For this purpose, the parameters of GP and GEP must be placed in the training dataset. Since more training dataset represents a better model and more testing data stands for better accuracy on testing results, we split the dataset 50–50% for training and testing (Sa et al., 2017). Accordingly, among sixteen trial datasets, eight sets were chosen for the training phase and the remaining eight sets were used for the testing phase in the GP and GEP modeling to assess the capability of these GAs versus restricted datasets (see Table 2).

3.2.1 Performance indicators

Here, the statistic factors including the mean absolute error (MAE), the mean squared error (MSE), and correlation coefficient (R) were used to check the accuracy of the recommended GP and GEP models in the training and testing phases:

$$\text{MAE} = \frac{\sum_{i=1}^{n}|h_i - t_i|}{n}, \tag{1}$$

$$\text{MSE} = \frac{\sum_{i=1}^{n}(h_i - t_i)^2}{n}, \tag{2}$$

$$\text{R} = \frac{(\sum_{i=1}^{n}(h_i - \overline{h_\iota})\,(t_i - \overline{t_\iota}))}{\sum_{i=1}^{n}(h_i - \overline{h_\iota})^2 \sum_{i=1}^{n}(t_i - \overline{t_\iota})^2} \tag{3}$$

where h_i and t_i are the real and the estimated output values for the ith specimen, respectively. Besides, n is the number of samples, $\overline{h_\iota}$ represents the mean of the actual values, and $\overline{t_\iota}$ stands for the mean of the predicted values. It is worth mentioning that if the model is a perfect fit for the data, then the R is 1, and MSE and MAE are 0. Thus, the R-value of much less than one and a higher MSE and MAE indicate a poorer prediction (Yong et al., 2020).

3.2.2 GEP-based models

As a common approach, the fitness function must first be selected to develop GEP-based models. For that reason, the fitness (f_i) of a given program (i) is initially measured by the following equation (Sarıdemir, 2010):

$$f_i = \sum_{j=1}^{C_t}(\text{M} - |C_{(i,j)} - T_j|), \tag{4}$$

where M, $C(i,j)$, and T_j are the selection range, the value got back by the individual chromosome i for fitness case j (out of C_t fitness cases), and the objective value for fitness case j. The benefit of this type of fitness functions is that the system can acquire the best possible solution for itself. Three input parameters comprising x_m, x_p, x_{tk} are entered as input variables and considered to construct the GEP model as input layers, while the output layers are set on σ_{YS}, σ_{UTS}, and δ. Figures 6-8 display the constructed ETs of the GEP approach models for σ_{YS}, σ_{UTS}, and δ based on the equations (5), (6), and (7), respectively, where the number of genes and the head length were ascertained after several trials for the GEP formulation.

$$\sigma_{YS} = \left[\left((\text{Cos}(x_{tk}) + x_p) - (x_{tk})\right) - \left(\ln\sqrt[3]{x_p}\right)\right] + \left[(x_p - 2.8) \times (9.33(x_{tk}))\right] + \left[(\text{Cos}(x_m + 9.5) \times x_p)\right], \tag{5}$$

$$\sigma_{UTS} = \left[(\text{Cos}(x_m{}^2 + 4.24)) \times \left(4.24 x_p - 18\right)\right] + \left[(x_m + 6) \times \left(\text{Sin}(x_m + 17) \times x_p\right)\right] + \left[(x_p - 20) \times \left(8.24 \times \text{Cos}(x_p)\right)\right] + \left[\left((\sin(x_{tk}) + 5.8) \times (46)\right) - \left(\log\sqrt{x_{tk}}\right)\right], \tag{6}$$

$$\delta = [(ArcTan((x_P)^2 - 0.88) - \cos(x_m))^3] + \left[\left(\sqrt[3]{\sin\frac{x_P}{x_m} + 405.22 + x_{tk}}\right) \times (x_m)\right] + \left[(x_P) \times \left(\cos\left((\cos(x_P)^3) \times (x_{tk} - x_m)\right)\right)\right] \tag{7}$$

As mentioned above, in these ETs, x_m, x_p, x_{tk} are the values for input layers, which are the SPD method, number of the pass, and temperature of the manufacturing process, respectively. Among sixteen datasets, 50% dataset was arbitrarily selected for the training segment and the residual set was employed for the testing phase to estimate the potential of GEP against limited datasets, which did not play any role in constructing the models (see Table 2). Lastly, the models with the best elongation to failure, the yield strength, and the ultimate tensile strength on both of the training and testing phases were chosen as the results of the runs. It can also be observed that 20, 45, and 30 number of chromosomes creates the best generation of individuals predicting the σ_{YS}, σ_{UTS}, and δ. The best GEP models with the well-adapted parameters were achieved following several runs, as presented in Tables 3-5. It should be noted that the selection of the set of terminals and functions are essential to generate the chromosomes, wherein the first one (terminal set) is composed of the independent variable, i.e. x_m, x_p, x_{tk}, and the second one contains some basic functions (power (x, y*), e, Log, Cos, Sin, Arc Tan) and (×, /, +, -) as four basic arithmetic operators.

Table 3. The parameters of GEP and GP corresponding to yield strength (σ_{YS}).

Method		Parameters	Value
GEP	General	Chromosomes	20
		Function set	×, /, +, -, power (x, y*), e, Cos, Sin
		Number of genes	4
		Head size	6
		Linking function	+
	Fitness Function	MSE	
	Genetic Operators	Mutation rate	0.09
		One-point recombination rate	0.2
		Two-point recombination rate	0.1
		Gene recombination rate	0.3
		Gene transportation rate	0.3
	Numerical Constant	Constants per gene	4
		Data type	Floating Point
		Lower bound	-10
		Upper bound	+10
GP	General	Number of population size	600
		Function set	+, -, ×, ÷, e, √, Arc Tan
		Value of reproduction	0.3
		Value of mutation	0.03
		Value of crossover	0.5
		Selection method	Roulette-wheel
		Type of initialization method	Half
		Number of generation	900
	Fitness function	MSE	

Table 4. The parameters of GEP and GP corresponding to ultimate tensile strength (σ_{UTS}).

Method		Parameters	Value
GEP	General	Chromosomes	45
		Function set	×, /, +, -, power (x, y*), Log, Sin, Cos
		Number of genes	3
		Head size	7
		Linking function	+
	Fitness Function	MSE	
	Genetic Operators	Mutation rate	0.03
		One-point recombination rate	0.5
		Two-point recombination rate	0.3
		Gene recombination rate	0.4
		Gene transportation rate	0.4
	Numerical Constant	Constants per gene	3
		Data type	Floating Point
		Lower bound	-10
		Upper bound	+10
GP	General	Number of population size	750
		Function set	+, -, ×, ÷, Sin, √, Log, Cos
		Value of reproduction	0.4
		Value of mutation	0.01
		Value of crossover	0.7
		Selection method	Roulette-wheel
		Type of initialization method	Half
		Number of generation	680
	Fitness function	MSE	

Table 5. The parameters of GEP and GP corresponding to elongation to failure (δ).

Method		Parameters	Value
GEP	General	Chromosomes	30
		Function set	$\times, /, +, -$, power (x, y^*), Arc Tan, Sin, Cos
		Number of genes	3
		Head size	8
		Linking function	+
	Fitness Function	MSE	
	Genetic Operators	Mutation rate	0.02
		One-point recombination rate	0.3
		Two-point recombination rate	0.5
		Gene recombination rate	0.2
		Gene transportation rate	0.2
	Numerical Constant	Constants per gene	5
		Data type	Floating Point
		Lower bound	-10
		Upper bound	+10
GP	General	Number of population size	600
		Function set	$+,-,\times,\div,e,\sqrt{}$, Arc Tan
		Value of reproduction	0.3
		Value of mutation	0.03
		Value of crossover	0.5
		Selection method	Roulette-wheel
		Type of initialization method	Half
		Number of generation	900
	Fitness function	MSE	

One of the main purposes of this work is to predict the objective parameters in the output layers using GEP, where this approach can be fulfilled just by utmost R or minimum MAE and MSE. In the present case, these obligations were satisfied by the following criteria:

For σ_{YS}, if the genes' number used is three (Sub-ETs), and linking function used is addition (+) (Figure 6). In the first sub-ET, it is observed that different functions such as $(\text{Cos}, +, -, \sqrt[3]{})$ have been applied. Moreover, inputs such as x_P and x_{tk} have been used to form the first sub-ET of the main ET of variable σ_{YS}. In the second sub-ET of the model, it can be seen that functions such as $(\times, -)$ have been utilized. Moreover, independent variables such as x_p and x_{tk} were used to formulate this sub-ET. In the last sub-ET $(\times, \text{Cos}, +)$ are the main functions. These functions and inputs such as x_P, and x_m are performed to structure the third sub-ET for formulating the σ_{YS} dependent variable.
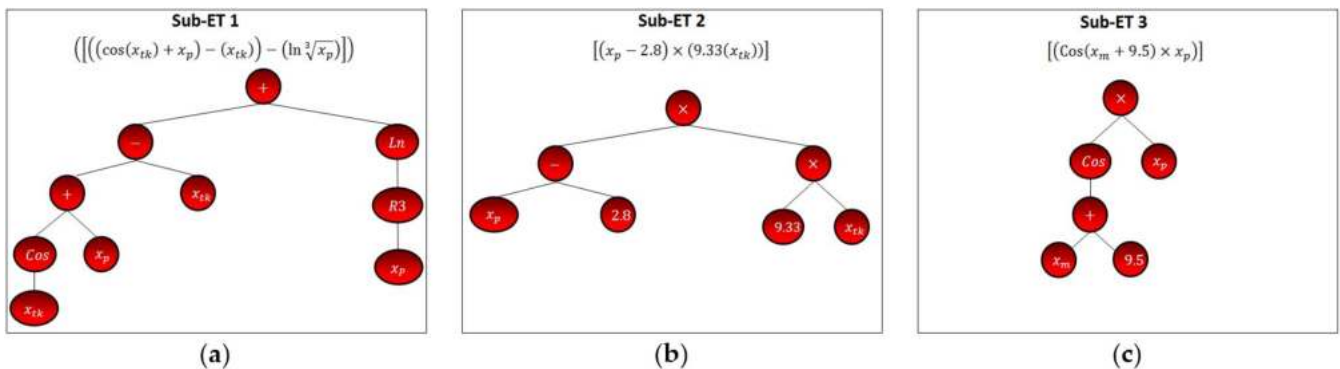

Figure 6. Expression tree of GEP model for the yield strength (σ_{YS}, MPa) as sub-ETs; (**a**) sub-ET 1, (**b**) sub-ET 2, and (**c**) sub-ET 3.

For σ_{UTS}, if the genes' number used is four (Sub-ETs), and linking function used is addition (+) (Figure 7). As is seen in this figure, in the first sub-ET, different functions such as (Cos, Power2,+, –, ×) have been applied. Moreover, inputs such as x_P and x_m have been used to form the first sub-ET of the main ET of variable σ_{UTS}. In the second sub-ET of the

model, it can be seen that functions such as $(\text{Sin}, +, \times)$ have been utilized. Moreover, independent variables such as x_m and x_p were used to formulate this sub-ET. In the third sub-ET of the model, it can be seen that functions such as $(\text{Cos}, -, \times)$ have been utilized. Moreover, just x_p as the independent variable was used to formulate this sub-ET. In the last sub-ET $(\text{Sin}, \text{Log}, -, +, \times, \sqrt{\ })$ are the main functions. These functions and input x_{tk} were performed to structure the third sub-ET for formulating the σ_{UTS} dependent variable.
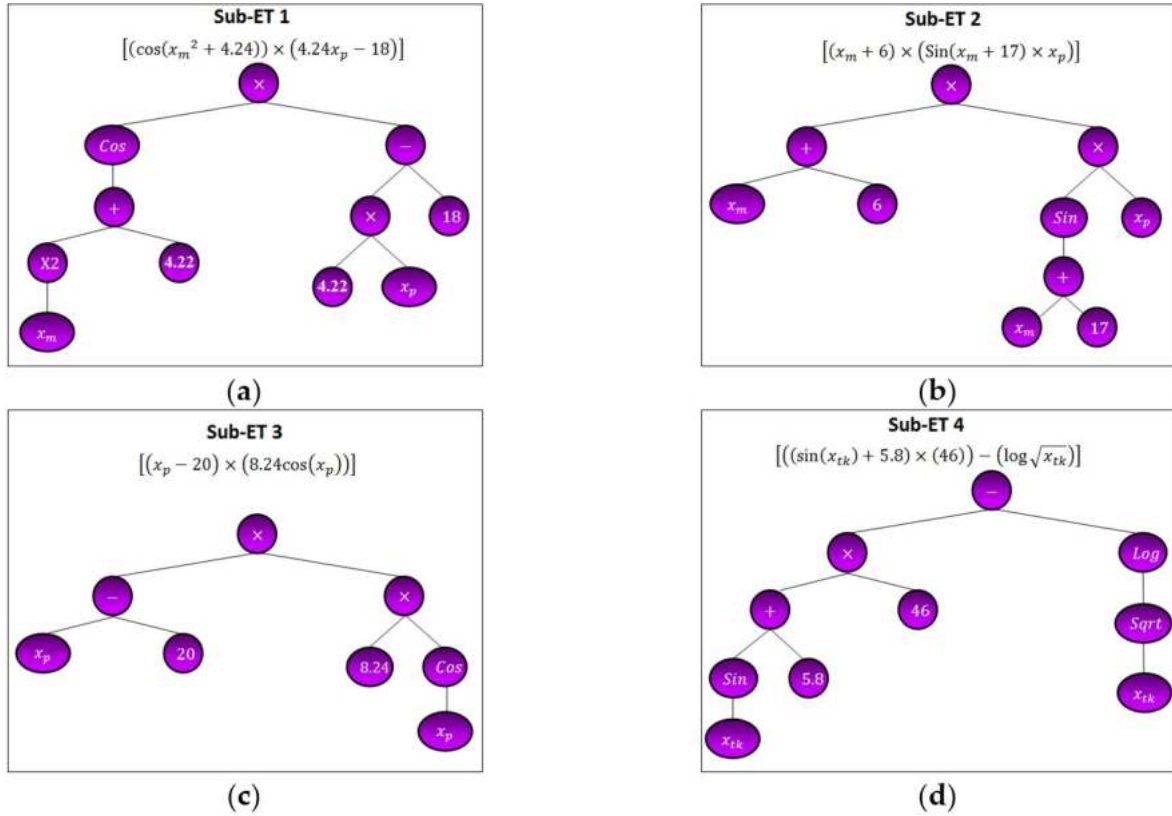

Figure 7. Expression tree of GEP model for the ultimate tensile strength (σ_{UTS}, MPa) as sub-ETs; (**a**) sub-ET 1, (**b**) sub-ET 2, (**c**) sub-ET 3, and (**d**) sub-ET 4.

For δ, if the genes' number used is three (Sub-ETs), and the linking function used is addition (+) (Figure 8). From this figure, different functions such as (Power 2, Power 3, Arc Tan, Cos, and $-$) have been employed. Also, inputs including x_P and x_m have been utilized to form the first sub-ET of the main ET of variable δ. In the second sub-ET of the model, it can be seen that functions for instance (Cube Root (R3), $\text{Sin}, +,/,\times$) have been utilized, where independent variables such as x_m, x_P, and x_{tk} were used to formulate this sub-ET. In the last sub-ET, $(\text{Cos}, -, +,\times)$ are the main functions. These functions and inputs, including x_m, x_P, and x_{tk} were employed to structure the third sub-ET for formulating the δ dependent variable.
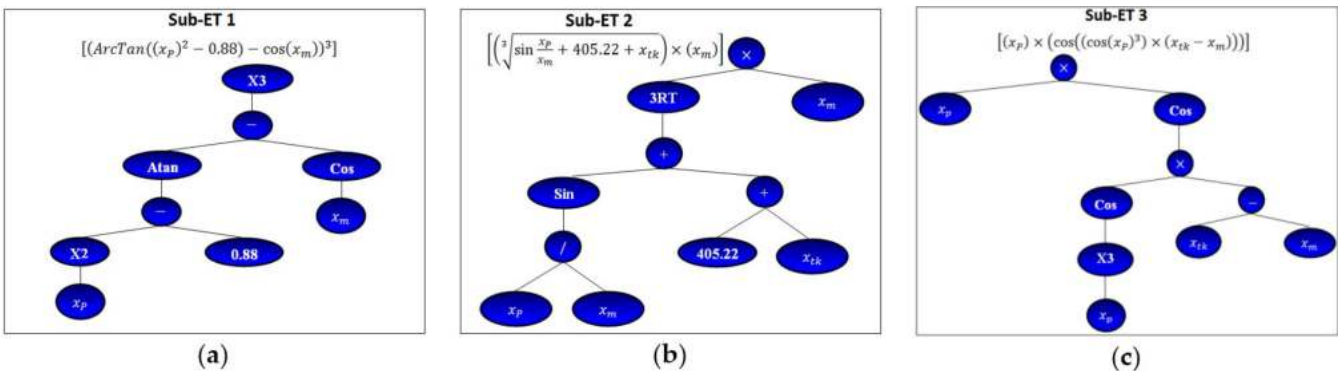

Figure 8. Expression tree of GEP model for the elongation to failure (δ, %) as sub-ETs; (**a**) sub-ET 1, (**b**) sub-ET 2, and (**c**) sub-ET 3.

Scatter plots of predicted versus measured values of the yield strength (σ_{YS}, MPa), the ultimate tensile strength (σ_{UTS}, MPa), and the elongation to failure (δ, %) of the processed ZK60 Mg alloy for GEP model in training and testing phases are illustrated in Figure 9. Figure 9a indicates that the model is accurate based on MSE, MAE, and R values. As it is observed, the MSE, MAE, and R of the model are 17.133, 7.088, and 0.93, respectively. After achieving the appropriate results in training, the rest 50% data set is applied to evaluate the predictive ability of the GEP model in estimating σ_{YS}, MSE, MAE, and R of the GEP model in prediction (unseen data set) reached 18.68, 3.55, and 0.99, respectively (Figure 9b). Figure 9c shows the accuracy of the proposed model for σ_{UTS} based on MSE, MAE, and R values in training. As it is observed, the error of the model is 172.4 for MSE and 10.768 for MAE, while the R-value of the model is 0.946. As shown in Figure 9d, MSE and MAE of the GEP model in prediction (unseen dataset) are 158.17 and 9.51, respectively, and R is 0.963 (more precise than the training segment). Figure 9e displays the accurateness of the model founded on MSE (13.51), MAE (3.275), and R (0.935). Similar to previous variables, after obtaining the fitting results in training, the rest 50% dataset is utilized to check the predictive capability of the GEP model in estimating δ. Figure 9f demonstrates that the model can predict the unseen dataset accurately.
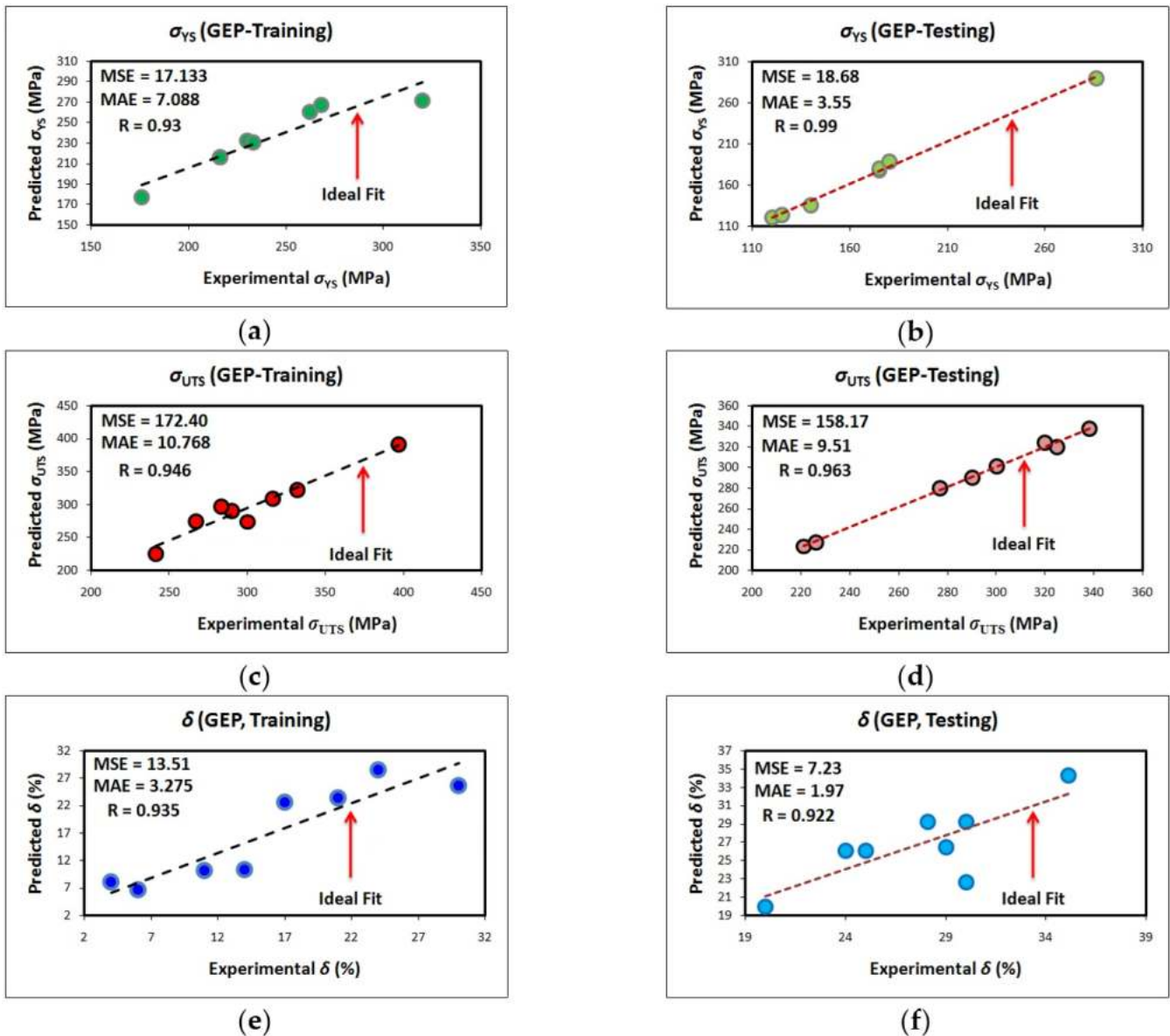

Figure 9. Scatter plots of predicted versus measured values of (**a,b**) the yield strength (σ_{YS}, MPa), (**c,d**) the ultimate tensile strength (σ_{UTS}, MPa), and (**e,f**) the elongation to failure (δ%) of the processed ZK60 Mg alloy for GEP model in training and testing phases.

3.2.3 GP-based models

One of the most frequent methods to illustrate the power of a predictive model is to compare the model with other predictive procedures. In the present work, we have employed GP, as the first EPML technique, to display the estimation power of the developed GEP model (Fallahpour et al., 2016). Accordingly, as one of the main goals of this study, precise mathematical models were developed by GP for the mechanical performance of the SPD-processed biodegradable ZK60 Mg alloy based on the above-mentioned input variables ($f(x_m, x_p, x_{tk})$), where GPLAB software was employed to run the GP model. It is found that the determination of the proper parameters for the GP is an error-based approach (Fallahpour et al., 2016). This shows that if the output is not desirable the parameters optimization process must be remade. As summarized in Tables 3-5, in the present work, the number of population size is 600, 750, and 600; function set is (+, -, ×, ÷, e, √, Arc Tan), (+, -, ×, ÷, Sin, √, Log, Cos), and (+, -, ×, ÷, e, √, Arc Tan); the reproduction value is 0.3, 0.4, and 0.3; the mutation value is 0.03, 0.01, and 0.03; the crossover value is 0.5, 0.7, and 0.5; fitness function is the mean squared error (MSE), the selection method is roulette-wheel, the initialization method type is Half, and the number of generation is 900, 680, and 900 for the σ_{YS}, σ_{UTS}, and δ, respectively. Finally, the mathematical predictors of σ_{YS}, σ_{UTS}, and δ using the GP algorithm are expressed as equations (8), (9), and (10), respectively. Once the equations were identified, the abilities of these models are assessed by applying the testing dataset in terms of MAE, MSE, as well as R. Figures 10-12 show the parse trees of the GP approach models for σ_{YS}, σ_{UTS}, and δ, respectively, wherein the number of the gene is three for all the GP formulations.

$$\sigma_{YS} = \left(\left(log\left(\sqrt{x_{tk}}\right)\right)^3 + x_p\right) + \left(\left((cos(x_m) + x_m)^3\right) \times \left(\frac{x_{tk}}{e^{x_m}}\right)\right) + (cos(x_{tk}) - x_m)^3, \tag{8}$$

$$\sigma_{UTS} = \left(x_p cos(x_m)^2\right) + (cos(x_m)x_m) + (sin(x_{tk}) - log(\sqrt{x_{tk}})), \tag{9}$$

$$\delta = \sqrt{x_{tk} + x_p - x_m} + ((sin(x_{tk})) + (x_p - sin(x_m))) + \left(x_m + \frac{e^{sin(x_{tk})}}{\sqrt{sin(x_m)+cos(x_p)}}\right) \tag{10}$$

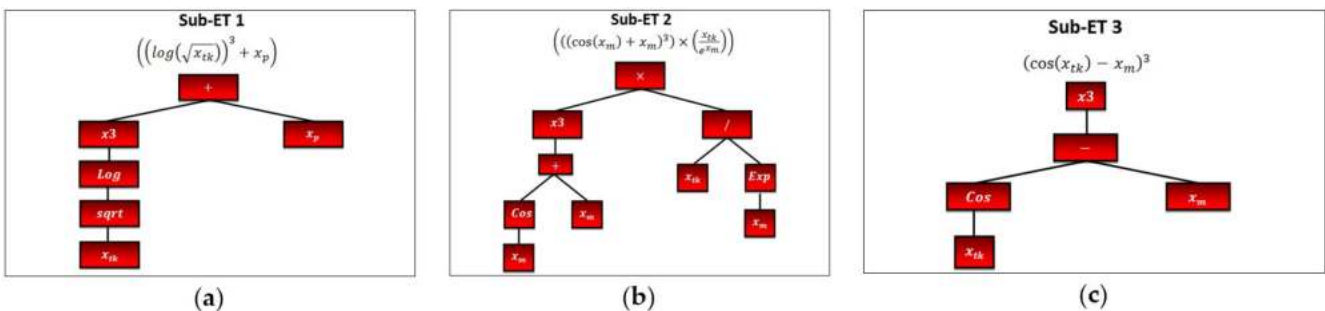**Figure 10.** Parse tree of GP model for the yield strength (σ_{YS}, MPa) as sub-ETs; (**a**) sub-ET 1, (**b**) sub-ET 2, and (**c**) sub-ET 3.
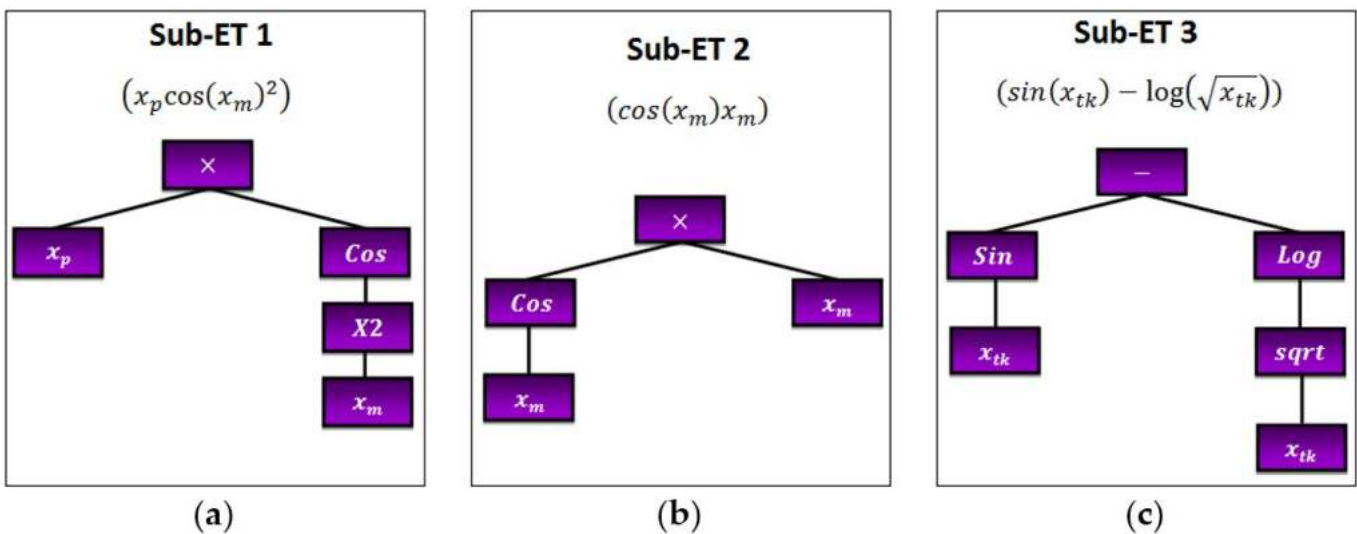

Figure 11. Parse tree of GP model for the ultimate tensile strength (σ_{YS}, MPa) as sub-ETs; (**a**) sub-ET 1, (**b**) sub-ET 2, and (**c**) sub-ET 3.
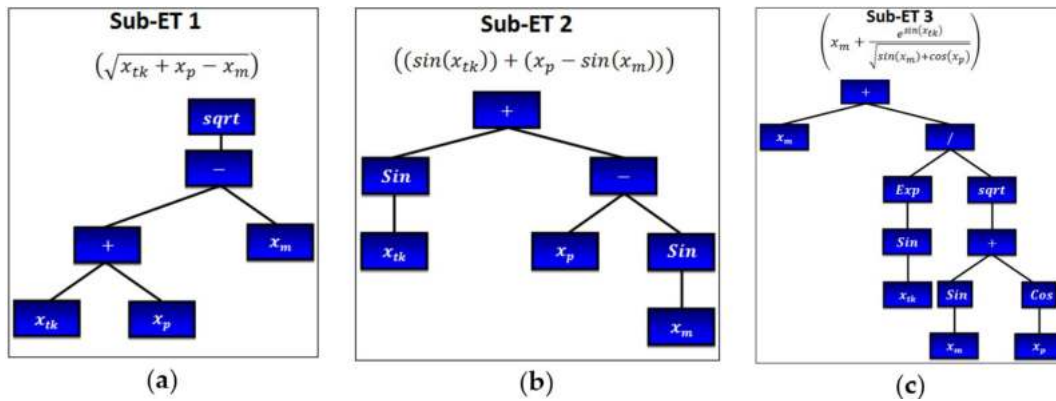
Figure 12. Parse tree of GP model for the elongation to failure (δ, %) as sub-ETs; (**a**) sub-ET 1, (**b**) sub-ET 2, and (**c**) sub-ET 3.

After the relationships were established, the robustness of the models was tested against the testing set. Figure 13 shows scatter plots of predicted versus measured values of the elongation to failure (δ, %), the yield strength (σ_{YS}, MPa), and the ultimate tensile strength (σ_{UTS}, MPa) of the processed ZK60 Mg alloy for GP model in training and testing phases, where the linear least-square fit line and the MAE, MSE, as well as R values, are illustrated for the training and testing sets. From Figure 13a, the values of MSE, MAE, and R for σ_{YS} in the training phase are 93.87, 15.986 and 0.873, respectively. Following the training segment, the remaining eight sets were employed for the testing phase to evaluate the predictive capability of the proposed models in measuring the mechanical behavior of the specimens. The statistical values of MSE, MAE, and R from testing in the GP model for σ_{YS} were found as 21.43, 11.08, and 0.902, respectively (Figure 13b). In the case of σ_{UTS}, MSE, MAE, and R values in the training phase are 189.23, 11.77, and 0.92, respectively (Figure 13c). These statistical values for σ_{UTS} in the testing phase were found to be 191.65, 13.51, and 0.918, as shown in Figure 13d. From Figure 13e, the values of MSE, MAE, and R for δ in the training phase are 19.33, 3.94, and 0.902, respectively. These statistical values for δ in the testing segment reached 11.23, 4.774, and 0.901, respectively (Figure 13f). This assessment corroborates that the proposed models are precisely founded on the values of MAE, MSE, and R.
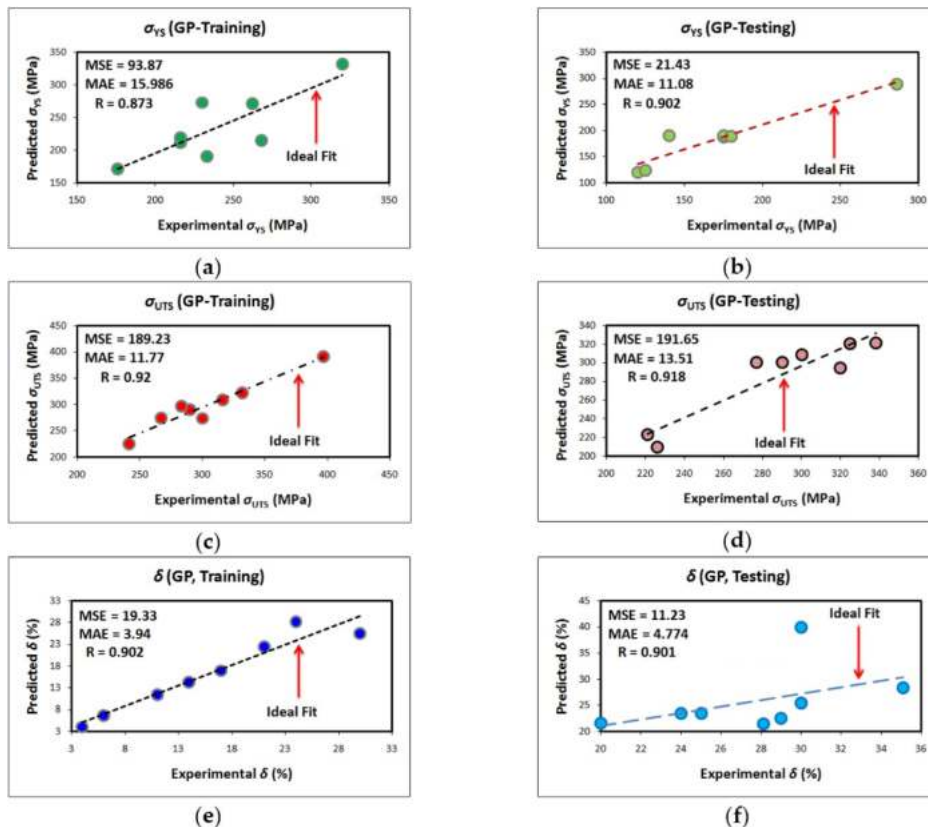

Figure 13. Scatter plots of predicted versus measured values of (**a,b**) the yield strength (σ_{YS}, MPa), (**c,d**) the ultimate tensile strength (σ_{UTS}, MPa), and (**e,f**) the elongation to failure (δ, %) of the processed ZK60 Mg alloy for GP model in training and testing phases.

4 DISCUSSION

4.1 Mechanical behavior of ZK60 Mg alloy

Referring to Figure 4a and bas well as Table 2, higher mechanical strength was detected at the second PTCAP pass as compared to other processed ZK60 Mg alloy. Since the mechanical behavior of the metallic implants principally counts on the microstructural features, so varying the microstructure of medical implant results in impressive alterations in the microhardness, mechanical strength, and ductility. In other words, the mechanical strength of UFG alloys can be controlled by the size of grains in accordance with the Hall–Petch relationship (Hansen, 2004):

$$\sigma = \sigma_0 + kg\bar{L}^{-1/2} \quad (11)$$

where σ is the yield stress at a mean linear intercept grain size $\bar{L}$, while σ_0 and kg are the Hall–Petch constants. It should be noted that this relationship is unsound as the grain size is less than 20 nm.

Based on our previous findings that the grain sizes of the PTCAP-processed ZK60 alloy are greater than 20 nm (Mesbah et al., 2019), we hypothesized that the improvement in the mechanical behavior of the ZK60-3 sample is attributed to a higher shear strain and a better microstructural refinement (a finer microstructure and a rise in the fraction of the region occupied by finer grains) during the PTCAP process (Faraji et al., 2012) compared to the other SPD processes, such as ECAP and high-ratio differential speed rolling (HRDSR) methods (Mostaed et al., 2014; Orlov et al., 2011). The other justification for improving the mechanical strength is the dissolution, fragmentation, and the rearrangement of the second phase, such as MgZn, $MgZn_2$, $ZrZn_2$, and $ZrZn_3$ (≤ 100 nm), during keeping time in the PTCAP channel and/or reheating between the passes. However, the drop in mechanical properties, despite the significant decrease in grain size in the ZK60-3, may have been caused by further development of the crystallographic defects like cracks and voids (Faraji et al., 2018).As evidenced in Figure 4c, although the PTCAP processing up to two passes has improved the ductility of the ZK60 alloy compared to the non-treated alloy, the percentage of improvement is lower than the other states. For instance, following one pass, δ raised from an initial value of 6% for the as-received alloy to around 11% and at the second pass reached a maximum of 14%, which shows a ~133% improvement in ductility, as compared to the non-treated alloy. However, in comparison with ZK60-14, which processed by 8 passes ECAP and showed a 485% improvement, the enhancement of ductility is not very impressive. In terms of the alloy composition, the obtained results also show that the biodegradable ZK60 Mg alloy processed by PTCAP with 2 passes possesses the highest mechanical strength as compared to the other TCAP and PTCAP processed Mg-based alloys like AZ31 and AZ91 (Abdolvand et al., 2017; Eftekhari et al., 2018). Also, from the Formability Index (*FI*) point of view, which can be estimated from the following relationship (Mesbah et al., 2019), the highest value of *FI* (5558 MPa%) was achieved in the case of biodegradable ZK60 Mg alloy processed by PTCAP with 2 passes. This discrepancy can be caused by the differences in primary grain size, the temperature of SPD processes, and texture development (Segal, 2018).

$$FI(MPA\%) = \sigma_{UTS}(MPA) \times \delta(\%) \quad (12)$$

where *FI*, $\sigma_{UTS,}$ and with δ are Formability Index, ultimate tensile strength, and elongation to failure, respectively. These results corroborate that among various types of biodegradable Mg-based alloys, the processed ZK60 Mg alloy by PTCAP with improved mechanical performance is the most promising candidate for use as a potential biodegradable implant material. However, the degradation rate of biodegradable ZK60 Mg alloy must be assessed and tuned in future works to meet an increase in load-bearing capacity of the supporting tissue and to sustain the mechanical integrity until the tissue is perfectly repaired. It is worth noting that in addition to characteristics of temporary implants (biological and mechanical properties), a patient must have an appropriate bone density and a robust immune system for successful implantation (Brar et al., 2009; Mariani et al., 2019; Pogorielov et al., 2017).

4.2 Statistical tests

Table 6 presents the assessment of the accuracy of the GEP models in terms of statistical tests. Following a rational assumption, it is argued that for |R| higher than 0.8, a robust correlation is present between the predicted and measured values (Smith, 1986). In all circumstances, the values of error, e.g. MAE and MSE, are supposed to at the lowest amount (Fallahpour et al., 2017). It should be mentioned that in the present study R is the root square of R^2. The achieved results corroborate that the proposed GEP-models have a very good performance on both of the training and testing datasets for all the three variables. More to the point, new factors recommended by Golbraikh and Tropsha (2002) were tested

out as the exterior corroboration of the models on the testing datasets. It is suggested that in any case one slope of the regression lines (k or k') through the origin must be close to 1 (Mollahasani et al., 2011). It should be mentioned that k and k' are the regression line slopes between the regressions of actual output (h_i) against predicted output (t_i) or t_i against h_i through the origin, i.e. $h_i = k\, t_i$ and $t_i = k'h_i$, respectively. Besides, the performance indexes of m and n as the two factors for assessing the performance of the model must be below 0.1. In addition to these indexes, another performance indicator, i.e. R_m is proposed (Roy and Roy, 2008), wherein the circumstance is fulfilled for $R_m > 0.5$. Either the squared correlation coefficient (through the origin) between predicted and experimental values ($R_o{}^2$), or the squared correlation coefficient between experimental and predicted values ($R_{o'}{}^2$) should be close to R^2 and to 1 (Alavi and Gandomi, 2011). Based on the given data in Table 6, the developed models gratify all of the obligatory circumstances, and thus this validation phase guarantees that the projected models are robustly proper and applicable.

Table 6. Statistical factors of the decision model for external validation.

Item	Formula	Condition	σ_{YS}	σ_{UTS}	δ
1	R	$0.8 < R$	0.99	0.963	0.922
2	$k = \dfrac{\sum_{i=1}^{n}(h_i \times t_i)}{h_i{}^2}$	$0.85 < k < 1.15$	1.11	1.01	0.995
3	$k' = \dfrac{\sum_{i=1}^{n}(h_i \times t_i)}{t_i{}^2}$	$0.85 < k' < 1.15$	1.04	1.007	1.003
4	$m = \dfrac{R^2 - R_o{}^2}{R^2}$	$|m| < 0.1$	0.013	0.041	0.022
5	$n = \dfrac{R^2 - R_{o'}{}^2}{R^2}$	$|n| < 0.1$	0.009	0.007	0.022
6	$R_m = R^2 \times \left(1 - \sqrt{\left|R^2 - R_o{}^2\right|}\right)$	$0.5 < R_m$	0.978	0.951	0.832

4.3 Comparison of GP and GEP models

As illustrated in Figures 9 and 13, the training set outcome verified that the proposed GEP and GP models have remarkably well learned the non-linear relationship between the input and the output variables with great solidarity and relatively low error values. Also, comparing the GEP and GP approach models prediction with the experimental consequences for the testing phase reveals a high generalization capability of the projected models and relatively low error values. This suggests the prosperous performance of the GEP and GP models for predicting the elongation to failure (δ, %), the yield strength (σ_{YS}, MPa), and the ultimate tensile strength (σ_{UTS}, MPa) of biodegradable Mg-based alloys as temporary orthopedic implants in training and testing phases. Figure 14 demonstrates the model comparison plots of the estimated values against the real data in support of GEP and GP models for δ, σ_{YS}, and σ_{UTS}. In fact, this figure makes available a synopsis on dissimilarities between the accurateness attained for disparate models in the testing phase. It is crystal clear from the graphs that both GEP and GP models do predict accurately the elongation to failure, the yield strength, and the ultimate tensile strength; however, the comparison between these models exhibits that the GEP model is more accurate than the GP model. This result is in good agreement with those available in the literature (ADMA, 2006; Faradonbeh et al., 2018). Therefore, it can be concluded that although both methods are capable of providing algebraic equations, the GEP approach model is more accurate than the GP procedure in estimating the mechanical properties of the processed ZK60 Mg alloy, especially for bone implant applications.
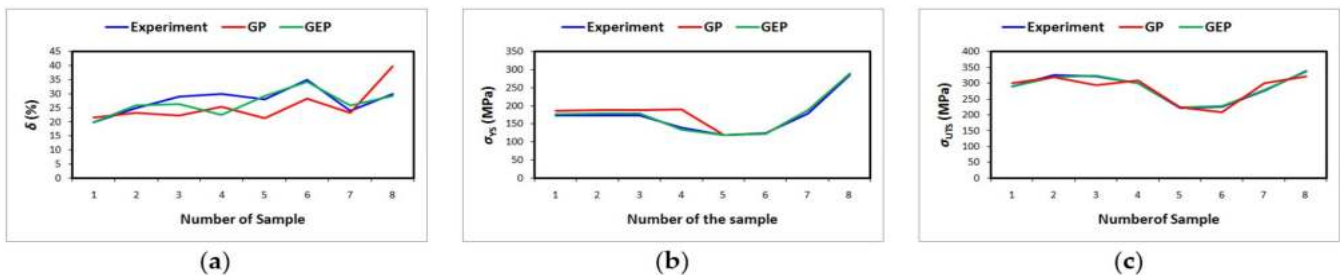

Figure 14. Model comparison plots of the estimated values against the real data for GEP and GP models, (**a**) the elongation to failure (δ, %), (**b**) the yield strength (σ_{YS}, MPa), and (**c**) the ultimate tensile strength (σ_{UTS}, MPa).

According to the results, it can be argued that GEP and GP as genetic algorithms are condemned to face one of two constraints: (i) if they are straightforward to manipulate genetically, they lose in functional complexity; (ii) if they have a specified amount of functional intricacy, they are very difficult to reproduce with modification (Koza, 1994). On the other hand, the manufacturing and processing of materials are subject to high uncertainty, which derives from characterization techniques and constraints in the accurateness of controlling the manufacturing process (Picklum and Beetz, 2019). In this context, variable selection and class imbalance is a challenging issue for the data mining community, it takes place as the specimens exhibiting one class is much lower than those presenting other classes. The easiest solution to prevail over this problem is to ensure that there is a balanced presentation of the members of each class present in the dataset, but this is an important task in the SPD-processed ZK60 Mg alloy as the lack of large well-arrange datasets severely restricts the amount, variety, as well as quality of data available. This is perhaps the most important limitation in the present study. Since the field of SPD of tube materials is comparatively young, the data mining results presented in this paper are very preliminary and their generalizability is questionable. Thus, the generalizability of GEP and GP models require a more extensive data set. This suggests that, as a major drawback, all empirical equations proposed in this research are presented only for a restricted range of datasets, which means that these equations did not have the capability of generalizing the mechanical performance of biodegradable ZK60 Mg alloy in biological environments and are still an issue open for further investigation.

5 CONCLUSIONS

This work aimed to propose an efficient approach for the formulation of the mechanical performance of the PTCAP-processed biodegradable ZK60 Mg alloy using GEP and GP. In this context, to verify the power of the predictive GEP model, the GP method was employed. Accordingly, two different GEP- and GP-based models were developed to predict the elongation to failure (δ, %), the yield strength (σ_{YS}, MPa), and the ultimate tensile strength (σ_{UTS}, MPa) of biodegradable Mg-based alloy as a temporary orthopedic implant, wherein the projected models were empirical as well as based on findings collected from the literature. Here, the SPD method, the number of the passes, and processing temperature were chosen as the input data, while σ_{YS}, σ_{UTS}, and δ of the processed alloys were selected as the output layer. The results of the training phase showed that the proposed GEP and GP models had well learned the non-linear relationship between the input and the output factors with great solidarity and relatively low error values. Moreover, the outputs of the testing segment corroborated a high generalization capacity of the projected models, wherein the accuracy of the models was assessed in terms of statistical values of MAE, MSE and R. The comparison between the proposed models revealed that the GEP model was accurate than the GP procedure and thus it can serve as a robust approach model for the new explicit formulation of the mechanical properties of numerous ultrafine-grained alloys for bone implant applications.

References

Abdolvand, H., Faraji, G., Karami, J.S., Baniasadi, M., 2017. Microstructure and mechanical properties of fine-grained thin-walled AZ91 tubes processed by a novel combined SPD process. Bulletin of Materials Science volume 40, 1471-1479.

Adir, O., Poley, M., Chen, G., Froim, S., Krinsky, N., Shklover, J., Shainsky-Roitman, J., Lammers, T., Schroeder, A., 2019. Integrating Artificial Intelligence and Nanotechnology for Precision Cancer Medicine. Advanced Materials 32, 1901989.

ADMA, 2006. Advanced data mining and applications: second international conference, ADMA 2006, Xi'an, China, August 14-16, 2006; proceedings. Springer.

Agarwala, S., Menon, A., Chaudhari, S., 2017. Cerclage Wiring as an Adjunct for the Treatment of Femur Fractures: Series of 11 Cases. Journal of orthopaedic case reports 7, 39-43.

Alavi, A.H., Gandomi, A.H., 2011. A robust data mining approach for formulation of geotechnical engineering systems. Engineering Computations: Int J for Computer-Aided Engineering 28, 242-274.

Azimi-Pour, M., Eskandari-Naddaf, H., 2018. ANN and GEP prediction for simultaneous effect of nano and micro silica on the compressive and flexural strength of cement mortar. Construction and Building Materials 189, 978-992.

Bahrami-Karkevandi, M., Nasiri-Tabrizi, B., Wong, K., Ebrahimi-Kahrizsangi, R., Fallahpour, A., Saber-Samandari, S., Baradaran, S., Basirun, W.J., 2019. Mechanochemistry approach to produce in-situ tungsten borides and carbides nanopowders: Experimental study and modeling. Materials Chemistry and Physics 224, 47-64.

Bazaka, K., Jacob, M.V., 2013. Implantable devices: issues and challenges. Electronics 2, 1-34.

Blanco-Justicia, A., Domingo-Ferrer, J., Martínez, S., Sánchez, D., 2020. Machine learning explainability via microaggregation and shallow decision trees. Knowledge-Based Systems 194, 105532.

Brar, H.S., Platt, M.O., Sarntinoranont, M., Martin, P.I., Manuel, M.V., 2009. Magnesium as a biodegradable and bioabsorbable material for medical implants. Jom 61, 31-34.

Byun, S.-H., Lim, H.-K., Lee, S.-M., Kim, H.-E., Kim, S.-M., Lee, J.-H., 2020. Biodegradable Magnesium Alloy (ZK60) with a Poly (l-lactic)-Acid Polymer Coating for Maxillofacial Surgery. Metals 10, 724.

Chakraborty Banerjee, P., Al-Saadi, S., Choudhary, L., Harandi, S.E., Singh, R., 2019. Magnesium implants: Prospects and challenges. Materials 12, 136.

Cilla, M., Borgiani, E., Martinez, J., Duda, G.N., Checa, S., 2017. Machine learning techniques for the optimization of joint replacements: Application to a short-stem hip implant. Plos one 12, e0183755.

Dargusch, M., Balasubramani, N., Venezuela, J., Johnston, S., Wang, G., Lau, C., Bermingham, M., Kent, D., StJohn, D., 2020. Improved biodegradable magnesium alloys through advanced solidification processing. Scripta Materialia 177, 234-240.

Davis, L., 1991. Handbook of genetic algorithms.

Ding, W., 2016. Opportunities and challenges for the biodegradable magnesium alloys as next-generation biomaterials. Regenerative biomaterials 3, 79-86.

Dumitru, F.-D., Higuera-Cobos, O.F., Cabrera, J., 2014. ZK60 alloy processed by ECAP: Microstructural, physical and mechanical characterization. Materials Science Engineering: A 594, 32-39.

Eftekhari, M., Fata, A., Faraji, G., Mashhadi, M., 2018. Hot tensile deformation behavior of Mg-Zn-Al magnesium alloy tubes processed by severe plastic deformation. Journal of Alloys and Compounds 742, 442-453.

Fallahpour, A., Olugu, E.U., Musa, S.N., Khezrimotlagh, D., Wong, K.Y., 2016. An integrated model for green supplier selection under fuzzy environment: application of data envelopment analysis and genetic programming approach. Neural Computing and Applications 27, 707-725.

Fallahpour, A., Wong, K.Y., Olugu, E.U., Musa, S.N., 2017. A predictive integrated genetic-based model for supplier evaluation and selection. International Journal of Fuzzy Systems 19, 1041-1057.

Faradonbeh, R.S., Hasanipanah, M., Amnieh, H.B., Armaghani, D.J., Monjezi, M., 2018. Development of GP and GEP models to estimate an environmental issue induced by blasting operation. Environmental monitoring assessment 190, 351.

Faraji, G., Babaei, A., Mashhadi, M.M., Abrinia, K., 2012. Parallel tubular channel angular pressing (PTCAP) as a new severe plastic deformation method for cylindrical tubes. Materials Letters 77, 82-85.

Faraji, G., Kim, H.S., Kashi, H.T., 2018. Severe plastic deformation: methods, processing and properties. Elsevier.

Figueiredo, R.B., Langdon, T.G., 2019. Processing Magnesium and Its Alloys by High-Pressure Torsion: An Overview. Advanced Engineering Materials 21, 1801039.

Golbraikh, A., Tropsha, A., modelling, 2002. Beware of q2! Journal of molecular graphics 20, 269-276.

González-Durruthy, M., Alberici, L.C., Curti, C., Naal, Z., Atique-Sawazaki, D.T., Vázquez-Naya, J.M., González-Díaz, H., Munteanu, C.R., 2017. Experimental–computational study of carbon nanotube effects on mitochondrial respiration: in silico

nano-QSPR machine learning models based on new Raman spectra transform with Markov–Shannon entropy invariants. Journal of chemical information modeling 57, 1029-1044.

Gopi, K., 2020. Impact of ECAP on wear performance of Al–Mn magnesium alloy. Materials Research Express 7, 016550.

Hansen, N., 2004. Hall–Petch relation and boundary strengthening. Scripta Materialia 51, 801-806.

He, Y., Pan, Q., Qin, Y., Liu, X., Li, W., Chiu, Y., Chen, J.J., 2010. Microstructure and mechanical properties of ZK60 alloy processed by two-step equal channel angular pressing. Journal of Alloys and Compounds 492, 605-610.

Heller, D.A., Shamay, Y., Shah, J., Isik, M., Budhathoki-Uprety, J., Roxbury, D., Sridharan, R., Chodera, J., Lowe, S., 2019. Development of Targeted Nanomedicines via Machine Learning Processes.

Itano, K., Ueki, K., Iizuka, T., Kuwatani, T., 2020. Geochemical Discrimination of Monazite Source Rock Based on Machine Learning Techniques and Multinomial Logistic Regression Analysis. Geosciences 10, 63.

Jones, D.E., Ghandehari, H., Facelli, J.C., 2016. A review of the applications of data mining and machine learning for the prediction of biomedical properties of nanoparticles. Computer methods programs in biomedicine 132, 93-103.

Kamrani, S., Fleck, C., 2019. Biodegradable magnesium alloys as temporary orthopaedic implants: a review. BioMetals 32, 185-193.

Kasaeian-Naeini, M., Hashemi, R., Hosseini, A., 2019. Lubrication performance of rapeseed oil-based nano-lubricants in parallel tubular channel angular pressing process. Journal of Central South University 26, 1042-1049.

Khoubrou, I., Nami, B., Miresmaeili, S.M., 2020. Investigation on the Creep Behavior of AZ91 Magnesium Alloy Processed by Severe Plastic Deformation. Metals and Materials International 26, 196–204.

Kim, H.-S., Moon, J.-H., Um, H.-Y., YOON, J.-i., Seung-Mi, B., 2020. Torsional severe plastic deformation method for metal bar, employing surface polishing to improve mechanical properties of metal bar. Google Patents.

Kim, W., Jeong, H., Jeong, H., 2009. Achieving high strength and high ductility in magnesium alloys using severe plastic deformation combined with low-temperature aging. Scripta Materialia 61, 1040-1043.

Koza, J.R., 1994. Genetic programming as a means for programming computers by natural selection. Statistics and Computing 4, 87-112.

Land, W.H., Schaffer, J.D., 2020. The Support Vector Machine, The Art and Science of Machine Intelligence. Springer, pp. 45-76.

Liu, C., Ren, Z., Xu, Y., Pang, S., Zhao, X., Zhao, Y., 2018. Biodegradable magnesium alloys developed as bone repair materials: a review. Scanning 2018.

Lu, W., Chen, Z., Huang, P., Yan, B., Yan, B., 2012. Microstructure, corrosion resistance and biocompatibility of biomimetic HA-based Ca-P coatings on ZK60 magnesium alloy. Int. J. Electrochem. Sci 7, 12668-12679.

Mariani, E., Lisignoli, G., Borzì, R.M., Pulsatelli, L., 2019. Biomaterials: foreign bodies or tuners for the immune response? Int J Mol Sci 20, 636.

Martynenko, N., Lukyanova, E., Serebryany, V., Prosvirnin, D., Terentiev, V., Raab, G., Dobatkin, S., Estrin, Y., 2019. Effect of equal channel angular pressing on structure, texture, mechanical and in-service properties of a biodegradable magnesium alloy. Materials Letters 238, 218-221.

McLachlan, S., Dube, K., Hitman, G.A., Fenton, N.E., Kyrimi, E., 2020. Bayesian Networks in Healthcare: Distribution by Medical Condition. arXiv preprint arXiv:.00224.

Mesbah, M., 2013. Producing ultra fine grain pure aluminum tubes using tubular channel angular pressing (TCAP)/Mohsen Mesbah. University of Malaya.

Mesbah, M., Faraji, G., Bushroa, A., 2014. Characterization of nanostructured pure aluminum tubes produced by tubular channel angular pressing (TCAP). Materials Science and Engineering: A 590, 289-294.

Mesbah, M., Fadaeifard, F., Karimzadeh, A., Nasiri-Tabrizi, B., Rafieerad, A., Faraji, G., Bushroa, A.R., 2016a. Nano-mechanical properties and microstructure of UFG brass tubes processed by parallel tubular channel angular pressing. Metals and Materials International 22, 1098-1107.

Mesbah, M., Faraji, G., Bushroa, A., 2016b. Electron back-scattered diffraction and nanoindentation analysis of nanostructured Al tubes processed by multipass tubular-channel angular pressing. Metals and Materials International 22, 288-294.

Mesbah, M., Fattahi, A., Bushroa, A., Faraji, G., Wong, K., Basirun, W., Fallahpour, A., Nasiri-Tabrizi, B., 2019. Experimental and Modelling Study of Ultra-Fine Grained ZK60 Magnesium Alloy with Simultaneously Improved Strength and Ductility Processed by Parallel Tubular Channel Angular Pressing. Metals and Materials International, 1-21.

Mollahasani, A., Alavi, A.H., Gandomi, A.H., 2011. Empirical modeling of plate load test moduli of soil via gene expression programming. Computers Geotechnics 38, 281-286.

Mostaed, E., Hashempour, M., Fabrizi, A., Dellasega, D., Bestetti, M., Bonollo, F., Vedani, M., 2014. Microstructure, texture evolution, mechanical properties and corrosion behavior of ECAP processed ZK60 magnesium alloy for biodegradable applications. Journal of the Mechanical Behavior of Biomedical Materials 37, 307-322.

Mueller, K., Mueller, S., 2007. Severe plastic deformation of the magnesium alloy AZ31. Journal of Materials Processing Technology 187, 775-779.

Mueller, T., Kusne, A.G., Ramprasad, R., 2016. Machine learning in materials science: Recent progress and emerging applications. Reviews in Computational Chemistry 29, 186-273.

Orlov, D., Raab, G., Lamark, T.T., Popov, M., Estrin, Y., 2011. Improvement of mechanical properties of magnesium alloy ZK60 by integrated extrusion and equal channel angular pressing. Acta Materialia 59, 375-385.

Picklum, M., Beetz, M., 2019. MatCALO: Knowledge-enabled machine learning in materials science. Computational Materials Science 163, 50-62.

Pogorielov, M., Husak, E., Solodivnik, A., Zhdanov, S., 2017. Magnesium-based biodegradable alloys: Degradation, application, and alloying elements. Interventional Medicine and Applied Science 9, 27-38.

Rafieerad, A., Bushroa, A., Nasiri-Tabrizi, B., Fallahpour, A., Vadivelu, J., Musa, S., Kaboli, S., 2016. GEP-based method to formulate adhesion strength and hardness of Nb PVD coated on Ti–6Al–7Nb aimed at developing mixed oxide nanotubular arrays. Journal of the mechanical behavior of biomedical materials 61, 182-196.

Rafieerad, A., Bushroa, A., Nasiri-Tabrizi, B., Kaboli, S., Khanahmadi, S., Amiri, A., Vadivelu, J., Yusof, F., Basirun, W., Wasa, K., 2017. Toward improved mechanical, tribological, corrosion and in-vitro bioactivity properties of mixed oxide nanotubes on Ti–6Al–7Nb implant using multi-objective PSO. Journal of the mechanical behavior of biomedical materials 69, 1-18.

Rao, X., Wu, Y., Pei, X., Jing, Y., Luo, L., Liu, Y., Lu, J., 2019. Influence of rolling temperature on microstructural evolution and mechanical behavior of AZ31 alloy with accumulative roll bonding. Materials Science and Engineering: A 754, 112-120.

Reshadi, F., Faraji, G., Aghdamifar, S., Yavari, P., Mashhadi, M.M., 2015. Deformation speed and temperature effects on magnesium AZ91 during tubular channel angular pressing. Materials Science and Technology 31, 1879-1885.

Roy, P.P., Roy, K., 2008. On some aspects of variable selection for partial least squares regression models. QSAR & Combinatorial Science 27, 302-313.

Sa, P.K., Bakshi, S., Hatzilygeroudis, I.K., Sahoo, M.N., 2017. Recent Findings in Intelligent Computing Techniques. Proceedings of the 5th ICACNI 1.

Sacha, G.M., Varona, P., 2013. Artificial intelligence in nanotechnology. Nanotechnology 24, 452002.

Sarıdemir, M., 2010. Genetic programming approach for prediction of compressive strength of concretes containing rice husk ash. Construction and Building Materials 24, 1911-1919.

Schmidt, J., Marques, M.R., Botti, S., Marques, M.A., 2019. Recent advances and applications of machine learning in solid-state materials science. npj Computational Materials 5, 1-36.

Segal, V., 2018. modes and processes of severe plastic deformation (SPD). Materials 11, 1175.

Smith, G.N., 1986. Probability and statistics in civil engineering. Collins professional and technical books 244.

Vinogradov, A., 2017. Effect of severe plastic deformation on tensile and fatigue properties of fine-grained magnesium alloy ZK60. Journal of Materials Research 32, 4362-4374.

Wang, L., Wu, S., Cao, G., Fan, Y., Dunne, N., Li, X., 2019. Biomechanical studies on biomaterial degradation and co-cultured cells: mechanisms, potential applications, challenges and prospects. Journal of Materials Chemistry B 7, 7439-7459.

Wang, P., Yin, T., Qu, S., 2020. On the grain size dependent working hardening behaviors of severe plastic deformation processed metals. Scripta Materialia 178, 171-175.

Wei, J., Chu, X., Sun, X.Y., Xu, K., Deng, H.X., Chen, J., Wei, Z., Lei, M., 2019. Machine learning in materials science. InfoMat 1, 338-358.

Yan, Z., Zhang, Z., Li, X., Xu, J., Wang, Q., Zhang, G., Zheng, J., Fan, H., Xu, K., Zhu, J., 2020. A novel severe plastic deformation method and its effect on microstructure, texture and mechanical properties of Mg-Gd-Y-Zn-Zr alloy. Journal of Alloys and Compounds, 153698.

Yang, J., Koons, G.L., Cheng, G., Zhao, L., Mikos, A.G., Cui, F., 2018. A review on the exploitation of biodegradable magnesium-based composites for medical applications. Biomedical Materials 13, 022001.

Yong, W., Zhou, J., Armaghani, D.J., Tahir, M., Tarinejad, R., Pham, B.T., Van Huynh, V., 2020. A new hybrid simulated annealing-based genetic programming technique to predict the ultimate bearing capacity of piles. Engineering with Computers, 1-17.

Zhou, T., Song, Z., Sundmacher, K., 2019. Big Data Creates New Opportunities for Materials Research: A Review on Methods and Applications of Machine Learning for Materials Design. Engineering 5, 1017-1026.